Deep learning approach to fractal surfaces: application to satellite images of urban areas

Delgadillo-Jimenez et al. *EPJ Data Science* (2026) 15:63
https://doi.org/10.1140/epjds/s13688-026-00660-3

EPJ Data Science

RESEARCH Open Access

Deep learning approach to fractal surfaces: application to satellite images of urban areas

Armando Delgadillo-Jimenez[1], Carina Toxqui-Quitl[1*], Raúl Castro-Ortega[1], Aldo Aguilar-Vallejo[1], Alfonso Padilla-Vivanco[1] and Anna Carbone[2]

Handling Editor: Efrat Blumenfeld Lieberthal

*Correspondence:
carina.toxqui@upt.edu.mx
[1]Computer Vision Laboratory, Universidad Politécnica de Tulancingo, Ingenierías 100, Hidalgo, 43629, Mexico
Full list of author information is available at the end of the article

Abstract

A Convolutional Neural Network (CNN) approach is proposed to quantify the Hurst exponent H of two-dimensional correlated random matrices. The approach (shortly referred to as **RegFractNet**) has been tested on deterministic and stochastic fractals and trained on large datasets of artificially generated two-dimensional Fractional Brownian fields. As real-world data, WorldView-2 (WV-2) high-resolution satellite images are considered. **RegFractNet** yields accurate estimates of the Hurst exponent H. As a further assessment of the **RegFractNet** robustness and accuracy, the outcomes are compared with those yield by standard methods as Detrending Moving Average (DMA), Box-Counting (BC), Variogram (VA) and Climacogram (CL) algorithms. A specific feature of the proposed **RegFractNet** approach, compared to standard approaches, is the ability to operate to 128×128 pixels size, essential to the implementation at small urban scales. As real world case study, the Hurst exponent H, estimated from WV-2 satellite imagery of urban areas, are fed in the relationship $D_f = 2 - H$. Fractal dimensions D_f are found to vary in the range $1.52 \div 1.93$ corresponding to less and high urbanized areas, thus confirming earlier studies.

Keywords: Convolutional Neural Network; Hurst exponent; Fractal dimension; Urban socio-technical systems; Detrending Moving Average algorithm

1 Introduction

Fractal geometry provides a powerful approach to feature self-similarity and scaling behaviour in terms of Hurst exponent H and fractal dimension D_f, which directly relate to changes in structure and environmental conditions of the investigated ecosystems. Morphology and function of cities are examples of fractals, with the fractal dimension D_f yielding a measure of urban concentration across scales [1–3]. Urban planners and geographers have recognized that spatial complexity is intimately related to social organization, featuring a variety of socio-economic-technological phenomena. Scaling behaviour has been related to the distribution of physical (such as roads, built-up areas) and socio-economic (such as gross domestic products, number of patents) features in urban contexts [4, 5]. A given urban feature Y can be linked to the population size N by a power law $Y \sim N^{\beta}$, with the exponent β depending on the fractal dimension D_f, thus bridging together urban scaling behaviour and fractal texture and opening new paths to the understanding of socio-economic phenomena and urban complex systems [6–9]. Fractal geometry and self-similarity concepts underlay the property of invariance under iteration, and describe how real world irregular fragmented structures, shapes and features emerge that traditional geometry could not do. Scaling relations of the form:

$$f(\lambda) \propto \lambda^{D_f} \quad , \tag{1}$$

are shown by self-similar textures where λ is a characteristic scale (a measuring unit size) and D_f is the fractal dimension that for self-similar processes writes as:

$$D_f = d - H \quad , \tag{2}$$

with d the Euclidean dimension and $H \in [0, 1]$ the Hurst exponent that quantifies roughness. $H > 0.5$ indicates persistent smooth random surfaces, $H < 0.5$ anti-persistent rough ones, and $H = 0.5$ corresponds to the ordinary Brownian function. Fractional Brownian fields, i.e. continuous functions of two variables $f_H(i_1, i_2)$ with the Hurst exponent H as a parameter, can be conveniently adopted for the description of fractal surfaces. As noted, Eq. (2) holds for self-similar processes, while fractal properties and power law correlations would imply generalized relationship and unrelated H and D_f values [10]. It is worth remarking that a central challenge in artificial intelligence and deep learning is to ensure that model outputs are interpretable and accessible beyond the circles of highly specialized scholars. The Hurst exponent, while well-established as a statistical descriptor of long-range dependence and surface roughness, might remain obscure to interpret and difficult to relate to the specific features of the system under investigation. By contrast, the fractal dimension provides a crystal geometric interpretation as a generalization of the Euclidean dimension d (point $d = 1$, surface $d = 2$, volume $d = 3$) to non-integer dimensions. In particular, in the two-dimensional case, the deviations of D_f from d offer a simple intuition of surface irregularity, enabling to interpret the CNN results in a tangible way and highlighting the potential of the **RegFractNet** model in the urban science context. Hence, in this work, the linear relationship Eq. (2) is adopted to derive the fractal dimension D_f from the Hurst exponent H rather than more sophisticated model (i.e. the modified Cauchy class [10]), that would introduce additional parameters and assumptions, preventing the direct connection between the estimated Hurst exponent and its geometric interpretation for the specific context of the urban science. Real-world data and in particular satellite imagery do not strictly satisfy self-similarity across all spatial scales. The derived fractal dimension should be interpreted as an approximate descriptor of surface properties within the scale range where self-similar behavior is observed. Hurst exponent H, fractal dimension D_f and scaling exponent β heavily depend on the models and variables chosen for their estimation. Hence, the improvement of theoretical models, computational protocols and related definitions is essential to the purpose of increasing accuracy and ultimately extending the range of scales i.e. from city blocks to metropolitan sizes. A detailed investigation of alternative models and relationships between Hurst exponent and fractal dimension, as well as their implications, is beyond the scope of the present work, mainly focused on providing a robust and efficient deep learning framework, supported by an explainable theoretical and practical description.

Fractal models have been widely employed in image processing for tasks such as texture analysis and classification. With advances in space science, remote sensing techniques have been introduced for monitoring and identifying earth resources on a large scale from data collected in digital form, readily accessible for computer-based processing. Fractal analysis can quantify the overall spatial complexity of remotely sensed images, with the advantage that fractal parameters are independent of the sensor properties [11, 12]. Fractal objects can be analyzed by machine learning and deep learning algorithms, which automatically extract features and uncover hidden patterns from high-dimensional heterogeneous data. Recent advances in deep learning have shown promising results in characterizing dynamical systems driven by Fractional Brownian Motion (FBM). Granik et al. [13] employed a deep learning model to estimate the Hurst exponent. Wentao et al. [14] use deep learning to identify the parameters of nonlinear dynamical systems driven by FBM. A deep learning technique for measuring the fractal dimension of the basins of attraction of the Duffing oscillator is proposed by Valle et al. [15]. However, the analysis of satellite imagery and urban fractal features using deep learning is currently unexplored.

In this work, a Convolutional Neural Network (CNN) approach (referred to as **RegFractNet** [16]) is put forward with the main purpose to estimate the Hurst exponent of satellite imagery of urban areas. **RegFractNet** is first trained and validated on FBM surfaces with known ground truth. This training and benchmarking strategy enables controlled experiments and precise error analysis. Afterward, the network model is tested on unseen synthetic deterministic (Koch curves, Sierpinski triangles) and stochastic fractals (FBM surfaces) to verify robustness and consistency of the Hurst exponent values. To further evaluate the **RegFractNet** performance, extensive comparisons with standard computational models (Detrending Moving Average (DMA), Box Counting (BC), Variogram (VA), and Climacogram (CL)) has been performed. A box-plot and an *Agreement Plot* (Bland-Altman analysis) are used to compare Hurst exponent values between them. The validated CNN model is applied to satellite imagery of urban areas (Prague, Torino, Vienna, Zurich) obtained from WorldView-2 (WV-2) [17]. Overall, the results demonstrate that the **RegFractNet** training model is capable of predicting the Hurst exponent from unseen artificial and real world fractals (satellite imagery of urban areas). Results are discussed and compared with the existing literature.

Last but not least, we note that the **RegFractNet** tool is publicly available [16] and operational either with the data used in this work or own data via an interactive web application and a MATLAB plug-in (https://sites.google.com/view/lvc-upt/available-plugins).

2 Methods and materials

The **RegFractNet** model and training, validating, and testing datasets are presented in Sects. 2.1 and 2.2. The computational steps and the architecture of the **RegFractNet** are described with further details in the Supplementary Materials.

For the sake of completeness, a brief description of the standard methods (namely Detrending Moving Average, Box Counting, Variogram and Climacogram algorithms) used for comparing the values of the Hurst exponents yield by **RegFractNet** is also included in Sect. 2.3.

2.1 CNN regression

Convolutional Neural Networks represent a powerful tool for extracting spatial patterns and features from fractal images, providing insights into the complex morphology of struc-

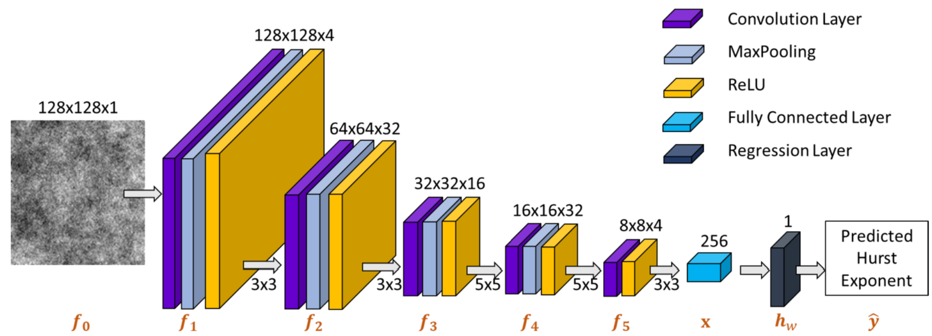

Figure 1 **RegFractNet** architecture

tures exhibiting deterministic and stochastic self-similarity. The CNN architecture consists of a sequential arrangement of layers as shown in Fig. 1. The input layer receives the data matrix (image map) $f_0 \in \mathbb{R}^{128\times128\times1}$.

The input layer is followed by f_l layers defined as a 2D convolution with a weight tensor W_l and a learnable bias term b_l. In the current configuration $l = 1:5$. In addition, the layers use a varying kernel sizes (3×3 and 5×5) and filter numbers (4, 32, 16, 32, 4). This architecture enables the capture of the complex spatial patterns related to the fractal structure of the images. Furthermore, a batch normalization layer (BN) and a Rectified Linear Unit (ReLU) activation function are included. After each convolutional block, a max-pooling subsampling layer with a window $T = 2 \times 2$ and a step of two is applied to avoid overlapping, reduce the spatial dimensions and control overfitting by retaining the most important features, allowing the network to learn deep representations of the texture and geometric complexity of the image [18]. After the convolutional layers, the output is first passed through a fully connected layer with 256 neurons to learn information. Backpropagation enables a feedforward network (which maps from $\mathbf{x}$ to $\hat{y}$) to expand linear models to nonlinear functions. So, the network architecture ends with a linear regression layer (h_w), which computes the loss function as the Mean Squared Error (MSE) between the predicted $\hat{y}$ and real target values y and provide the final prediction $\hat{y}$ of the Hurst exponent (H) value. The full set of **RegFractNet** equations and further details are reported in the Sect. 1 of the Supplementary Material.

The proposed model is implemented on MATLAB R2023b by using the Deep learning toolbox [19]. The Convolutional Neural Network is generated and tested by means of the *trainNetwork* MATLAB function. The CNN training process is performed by the Adam optimizer with an initial learning rate $\epsilon = 0.01$ and carried out over 20 *epochs*, with a mini-batch size of 32 [18]. The data are shuffled at every epoch to ensure that the learned representations help the model generalize. This architecture enables the capture of complex, nonlinear relationships between the texture patterns of images and the corresponding Hurst parameter, providing an efficient alternative to traditional methods (such as BC, DMA, VA, CL) frequently used in fractal analysis [20].

2.2 CNN training, validation and testing

To evaluate the generalization capability of the proposed **RegFractNet** model, it is important to ensure that the model performs well first on training and validation data and then on unseen data. For these purposes, the following sets of data are considered:

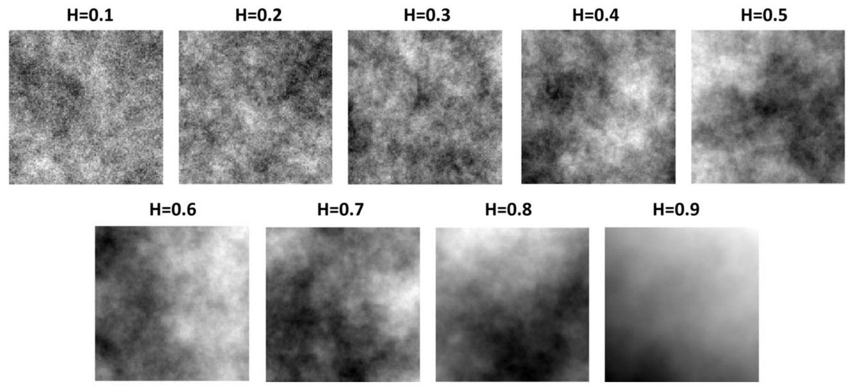

Figure 2 Fractional Brownian Surfaces samples with size 128 × 128 and controlled Hurst exponent H ranging from 0.1 to 0.9 with step $\Delta H = 0.1$

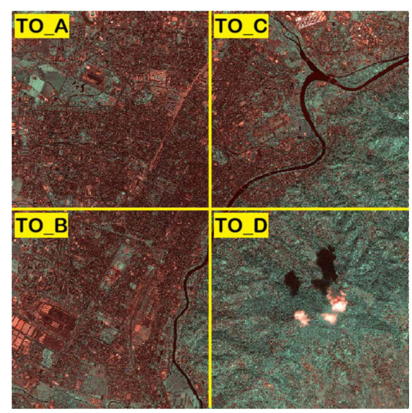

Figure 3 Image N45-024 (Torino) of the WV-2 [17] collection shown in false color. Urban infrastructure components (such as buildings, roads) are shown in orange color, whereas vegetation components (such as grasses, forestlands) in cyan. Each *RoI* spans diverse land use patterns, ranging from densely constructed city centers to peripheral vegetated zones

- Training and Validation Data (FBM surfaces). The model learns patterns from artificial fractal data by adjusting its parameters and labeling each one. The validation data set is used to assess the performance of the regression model during training and its ability to handle unknown data before final testing. A dataset of 3990 artificial fractal images is generated by the Cholesky-Levinson factorization (CLF), implemented via FRACLAB [21]. Synthetic images are obtained with controlled Hurst exponent H values ranging from 0.05 to 0.95 with step ΔH = 0.05. The spatial resolution of the 2D fractal surfaces is 128 × 128 gray-level pixels. Figure 2 shows fractal surface samples used to train the neural network. The dataset is randomly shuffled, 95% was used for training and the remaining 5% for validation.
- Testing Data (Satellite Imagery). High-resolution satellite images with varying levels of built-up density are used as further testing dataset. A given Region of Interest (*RoI*) encompasses urban sectors of the four European cities, with spatial resolution of $10.73\,m$ and covers approximately $120.72\,km^2$ for each city. Each image is divided into four sub-images of size 512 × 512 pixels, delimited by yellow lines and labeled by A, B, C, and D. In Fig. 3, the WV-2 N45-024 image (*RoI* Torino city) is shown in false color. The primary information and statistics regarding all satellite images used in the analysis, are also reported in the Sect. 2 of the Supplementary materials.

2.3 Standard methods

To assess robustness and accuracy of **RegFractNet**, an extensive comparison is performed against the outcomes of standard numerical algorithms (such as the Detrending Moving Average (DMA), Box Counting (BC), Variogram (VA), Climacogram (CL)). Most of the algorithm codes are available in FRACLAB [21] and MATLAB [19]. For the sake of completeness, a brief description of these standard approaches is provided here below.

2.3.1 Detrending Moving Average (DMA)

The *Detrending Moving Average* algorithm operates via a generalized high-dimensional variance σ_{DMA} of $f_H(r)$ around the moving average function $\tilde{f}_H(r)$ [22], that, for $d = 2$, writes:

$$\sigma^2_{DMA} = \frac{1}{(N_1 - n_{1_{max}})(N_2 - n_{2_{max}})} \times \sum_{i_1=n_1}^{N_1} \sum_{i_2=n_2}^{N_2} [f(i_1,i_2) - \tilde{f}_{n_1 n_2}(i_1,i_2)]^2 \quad , \tag{3}$$

with $\tilde{f}_{n_1 n_2}(i_1,i_2)$ given by:

$$\tilde{f}_{n_1 n_2}(i_1,i_2) = \frac{1}{n_1 n_2} \times \sum_{k_1=0}^{n_1-1} \sum_{k_2=0}^{n_2-1} f(i_1 - k_1, i_2 - k_2) \quad . \tag{4}$$

First, the average scalar field $\tilde{f}_{n_1 n_2}(i_1,i_2)$ is estimated over sub-arrays with different size $n_1 \times n_2$. Next the difference $f(i_1,i_2) - \tilde{f}_{n_1,n_2}(i_1,i_2)$ for each sub-array $n_1 \times n_2$ is calculated. It can be shown that Eq. (3) behaves as:

$$\sigma^2_{DMA} \sim \left[\sqrt{n_1^2 + n_2^2}\right]^{2H} = s^H \quad . \tag{5}$$

Hence, the log-log plot of σ^2_{DMA} vs. $s = n_1^2 + n_2^2$ yields a straight line with slope H.

2.3.2 Box Counting (BC)

The *Box-Counting* method is widely adopted for quantifying fractal objects. The MATLAB function [19, 23] is used for the estimates carried on in this work. Grids of size Υ are mapped to the surface to be analyzed. The grids are subdivided into equal-sized cells ε that become progressively smaller. The number of boxes $N(\varepsilon)$ that contain information about the object is counted. The fractal dimension according to the *Box-Counting* method is defined as:

$$D_f = \frac{\log(N(\varepsilon))}{\log(\Upsilon/\varepsilon)} \tag{6}$$

2.3.3 Variogram (VA)

The *Variogram*, widely used for spatial analysis in geostatistics, is defined as the squared increment from a point to its lag distances k_1 and k_2 [24]:

$$\gamma = \frac{1}{N_1(k_1)N_2(k_2)} \sum_{i_1=1}^{N_1(k_1)} \sum_{i_2=1}^{N_2(k_2)} \left\{[\, V(i_1,i_2) - V(i_1+k_1,i_2)\,]^2 + [\, V(i_1,i_2) - V(i_1,i_2+k_2)\,]^2\right\} \tag{7}$$

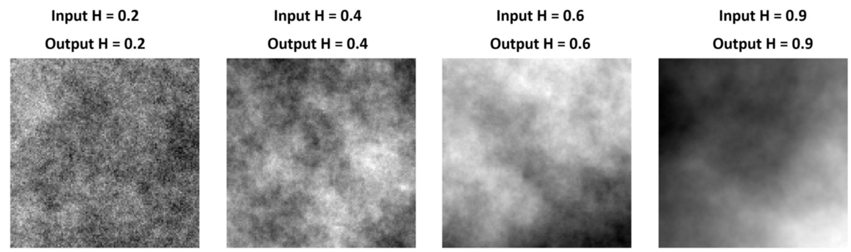

Figure 4 Fractional Brownian Surfaces external at **RegFractNet**. Input and output H values are reported on top of each image

where $N_1(k_1)$ and $N_2(k_2)$ are the numbers of pairs at each respective lag distance k_1 and k_2, $V(i_1, i_2)$, $V(i_1 + k_1, i_2)$ and $V(i_1, i_2 + k_2)$ are the sample values at positions i_1, i_2 and $i_1 + k_1, i_2 + k_2$, respectively. The slope of the log-log plot of γ vs. the lag distances k_1 and k_2 is found to be proportional to $2H$.

2.3.4 Climacogram (CL)
The *Climacogram* estimator is defined at each coordinate pair of a 2D matrix as [25]:

$$\hat{\gamma}(\kappa_1, \kappa_2) = \frac{1}{n^2/\kappa^2 - 1} \sum_{i_1=1}^{n/\kappa_1} \sum_{i_2=1}^{n/\kappa_2} (f_{i_1,i_2}^{(\kappa)} - \bar{f})^2 \tag{8}$$

where n is the number of intervals along each spatial direction, $\kappa = \sqrt{\kappa_1 \kappa_2}$, with $\kappa_1 = k_1/\Delta$ and $\kappa_2 = k_2/\Delta$ the dimensionless spatial scales with Δ the discretization unit (i.e. pixel length), $f_{i_1,i_2}^{(\kappa)} = \frac{1}{\kappa^2} \sum_{\psi=\kappa_1(i_2-1)+1}^{\kappa_1 i_2} \sum_{\xi=\kappa_2(i_1-1)+1}^{\kappa_2 i_2} f_{\xi,\psi}$ is the space-averaged process at scale κ, and $\bar{f} = \sum_{i_1,i_2=1}^{n} \bar{f}_{i_1,i_2}/n^2$. The scaling behaviour can be obtained through the log-log slope of $\hat{\gamma}(\kappa)$.

3 Results

In this section, the proposed **RegFractNet** approach is implemented to estimate the Hurst exponent of synthetic and real datasets. To further evaluate accuracy and robustness of the **RegFractNet** network model, a comparison is made by using the methods described in the previous section. For the sake of completeness, the comparison is also performed by using deterministic fractals (results reported in Sect. 3 of the Supplementary Materials).

3.1 Fractional Brownian surfaces

A dataset of 3990 grayscale images of simulated Brownian surfaces, each with 128×128 pixels size, is fed in to **RegFractNet**. The Brownian surfaces are randomly shuffled, 95% was used for training and the remaining 5% for validation. Figure 4 shows some results obtained using the **RegFractNet** to predict the Hurst exponent value of external FBM surfaces.

3.2 WV-2 imagery

The trained model is used to estimate the Hurst exponent of unseen satellite images. To this scope, the selected urban areas must match the input dimensions used during training, specifically 128×128 pixel grayscale images. Therefore, the 4 subareas A, B, C, and D

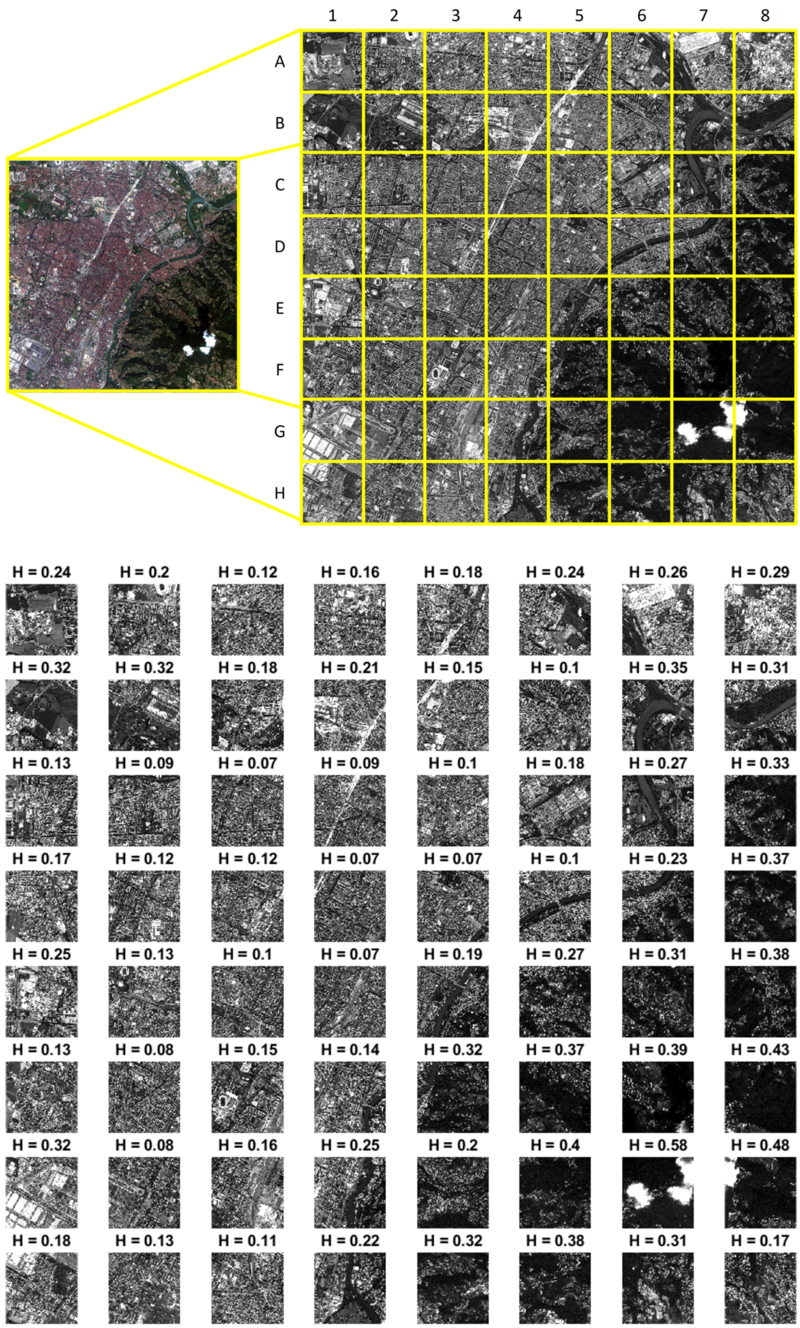

Figure 5 Top left: Image N45-024 (Torino). Top right: 64 fixed-size non-overlapping patches, each measuring 128 × 128 pixels, extracted from image N45-024. The red band is selected for testing and arranged into a matrix outlined in yellow, labeled with letters (A–H) for rows and numbers (1–8) for columns, in order to identify the different sections of the *RoI*. Bottom: Hurst exponents yield by the **RegFractNet** model for each of the 64 patches

(Fig. 3) are split into 16 fixed-size non-overlapping patches of 128 × 128 pixels (top-right panel of Fig. 5). The Hurst exponent values yield by the **RegFractNet** for the 64 urban areas are shown in the bottom panel of Fig. 5. For regions with high urban density, the **RegFractNet** model gives low values of H. As the level of urbanization decreases, a no-

Table 1 Fractal dimension D_f for the eight sectors of the WV-2 images of Torino labelled by capital letters (first column). The fractal dimensions are calculated by using the Hurst exponent yield respectively by **RegFractNet** [1], Detrending Moving Average [2], Box Counting [3], Variogram [4] and Climacogram [5]

Areas	D_f[1]	D_f[2]	D_f[3]	D_f[4]	D_f[5]	Areas	D_f[1]	D_f[2]	D_f[3]	D_f[4]	D_f[5]
A1	1.76	1.86	1.86	1.88	1.25	E1	1.75	1.87	1.88	1.87	1.28
A2	1.80	1.87	1.88	1.90	1.33	E2	1.87	1.88	1.88	1.93	1.46
A3	1.88	1.87	1.89	1.96	1.49	E3	1.90	1.88	1.88	1.97	1.52
A4	1.84	1.88	1.89	1.92	1.41	E4	**1.93**	**1.89**	**1.89**	**1.97**	**1.54**
A5	1.82	1.87	1.88	1.91	1.37	E5	1.81	1.87	1.87	1.97	1.37
A6	1.76	1.86	1.88	1.89	1.34	E6	1.73	1.87	1.85	1.93	1.40
A7	1.74	1.85	1.88	1.90	1.15	E7	1.69	1.86	1.84	1.91	1.43
A8	1.71	1.87	1.88	1.90	1.29	E8	1.62	1.86	1.80	1.92	1.35
B1	1.68	1.84	1.83	1.86	1.20	F1	1.87	1.87	1.88	1.92	1.42
B2	1.68	1.88	1.86	1.89	1.26	F2	1.92	1.88	1.89	1.98	1.61
B3	1.82	1.88	1.88	1.92	1.37	F3	1.85	1.87	1.88	1.94	1.37
B4	1.79	1.87	1.88	1.93	1.32	F4	1.86	1.88	1.88	1.94	1.43
B5	1.85	1.88	1.89	1.93	1.37	F5	1.68	1.87	1.84	1.92	1.31
B6	1.90	1.86	1.88	1.97	1.48	F6	1.63	1.87	1.80	1.94	1.34
B7	1.65	1.85	1.84	1.90	1.28	F7	1.61	1.86	1.77	1.90	1.26
B8	1.69	1.85	1.83	1.91	1.24	F8	1.57	1.83	1.69	1.90	1.33
C1	1.87	1.87	1.88	1.93	1.42	G1	1.68	1.86	1.88	1.86	1.25
C2	1.91	1.88	1.88	1.94	1.52	G2	1.92	1.88	1.89	1.95	1.54
C3	**1.93**	**1.88**	**1.89**	**1.98**	**1.67**	G3	1.84	1.87	1.88	1.94	1.27
C4	1.91	1.88	1.89	1.97	1.41	G4	1.75	1.87	1.88	1.92	1.27
C5	1.90	1.88	1.89	1.98	1.51	G5	1.80	1.87	1.85	1.94	1.36
C6	1.82	1.87	1.88	1.92	1.33	G6	1.60	1.86	1.78	1.92	1.34
C7	**1.73**	**1.87**	**1.86**	**1.90**	**1.36**	G7	**1.42**	**1.76**	**1.79**	**1.58**	**1.05**
C8	1.67	1.84	1.82	1.93	1.29	G8	**1.52**	**1.83**	**1.77**	**1.84**	**1.06**
D1	1.83	1.88	1.88	1.94	1.49	H1	1.82	1.86	1.88	1.91	1.23
D2	1.88	1.88	1.89	1.94	1.43	H2	1.87	1.87	1.88	1.94	1.48
D3	1.88	1.88	1.89	1.97	1.49	H3	1.89	1.88	1.88	1.94	1.49
D4	1.93	1.89	1.89	1.97	1.56	H4	1.78	1.86	1.86	1.89	1.30
D5	1.93	1.89	1.89	1.97	1.48	H5	1.68	1.87	1.83	1.92	1.30
D6	1.90	1.88	1.88	1.98	1.39	H6	1.62	1.88	1.81	1.90	1.33
D7	1.77	1.87	1.85	1.93	1.28	H7	1.69	1.86	1.84	1.88	1.25
D8	1.63	1.87	1.81	1.87	1.32	H8	1.83	1.87	1.86	1.93	1.40

ticeable shift in the predicted value occurs, reflected by increasing H values. In Table 1, the fractal dimension estimated by using the linear relationship $D_f = 2 - H$ vary in the range $1.52 \div 1.93$, consistently with the values reported earlier in the literature [9, 26–28].

Accuracy and robustness of the **RegFractNet** in predicting the Hurst exponent value of unseen satellite images are checked against the standard methods described in Sect. 2.3. Figure 6 illustrates one of the analyzed urban areas (image N45-024 Torino). As shown, Sections A and B are highly urbanized, with a high concentration of buildings and infrastructure, while Sections C and D are the least urbanized. Hurst exponent H and related fractal dimension D_f are obtained using the two-dimensional DMA on the red band of the WorldView-2 (WV-2) satellite images [22]. The σ_{DMA} results are plotted in $log - log$ scale. The DMA algorithm has been implemented for $n_1 = n_2$, $n_1 \in [2, 49]$, with $\Delta n_1 = 1$, according to Eq. (5). It is evaluated individually on each sub-image to get the variability of the scaling properties of different areas. Regressions are computed within the range

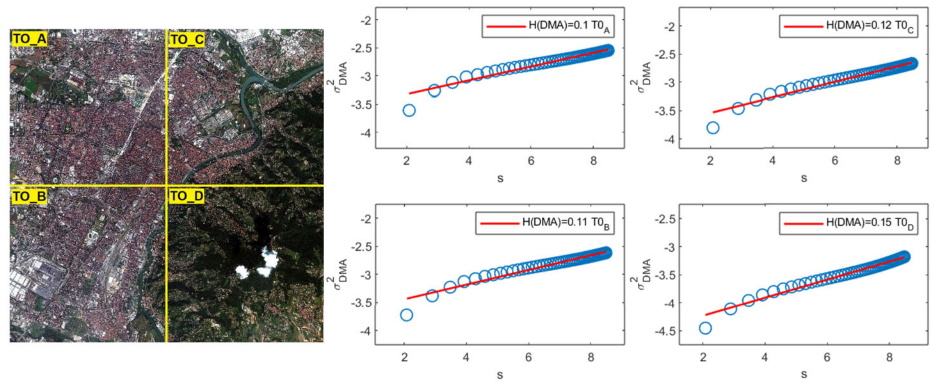

Figure 6 (Left panel) Image N45-024 (Torino) downloaded from the *Urban Atlas* largest European Cities collection of WorldView-2 [17]. (Right panel) Log-log plots of σ^2_{DMA} for each sub-image of size 512 × 512 pixels. Estimated H are obtained as the slope of the regression line by least squares

($2 < s < 8.5$), providing an estimate of H. The Hurst exponent tends to be lower for urbanized areas. On the contrary, its value is the highest for dispersed areas. As can be seen in Fig. 6, the Hurst exponent effectively provides insight into the variation of urban and sub-urban sections within a single region and across multiple cities.

For each sub-image, the DMA algorithm is implemented separately to grasp the variability in the scaling properties across different areas. Results for other standard methods and cities can be found in the Supplementary Material, Sect. 4 and 5. As expected, higher D_f values generally correspond to more densely populated areas and larger built-up surfaces (see also [9, 26]).

4 Discussion

To evaluate the performance of the network model, we have considered regions, measuring 1024 × 1024 pixels, split into four sections of 512 × 512 pixels each and then further split into 16 fixed-size non-overlapping patches of 128 × 128 pixels, matching the input size supported by the neural network. The variability in urbanization degree has been quantified using the fractal dimension ($D_f = 2 - H$) for four European cities from the WorldView-2 (WV-2) satellite image collection database. By comparing the results obtained for these cities, we can observe variations across different urban contexts, highlighting differences in historical development, land-use patterns, and spatial organization. Hurst exponents (H) consistent with the observed urbanization levels are obtained for the 64 patches of the satellite image. Specifically, highly urbanized areas tend to exhibit lower H values, while regions with low construction density exhibit higher H values. For each 512 × 512 sub-area analyzed via DMA, the average of the corresponding H values predicted by **RegFractNet** is computed. The average H values obtained by the network exhibit a trend that aligns closely with the results of the DMA analysis. Table 2 shows the fractal dimension estimated by using the linear relationship $D_f = 2 - H$.

In order to further clarify the relationship between fractal dimension, morphological complexity, and level of urbanization, we have expanded our analysis by explicitly comparing areas with both similar and different D_f values across multiple cities, as illustrated in Fig. 7. As shown, urban regions from different cities (Torino, Prague, Vienna and Zurich)

Table 2 Fractal dimension D_f for the WV-2 sections of Prague, Torino, Vienna, and Zurich. The values of D_f are estimated by entering the Hurst exponent yield respectively **RegFractNet** [1], Detrending Moving Average [2], Box Counting [3], Variogram [4] and Climacogram [5] into the linear relationship $D_f = 2 - H$

VW-2 Image	Sections	D_f[1]	D_f[2]	D_f[3]	D_f[4]	D_f[5]
Prague N50-090	A	1.72	1.82	1.83	1.75	1.12
	B	1.74	1.85	1.72	1.93	1.26
	C	1.75	1.88	1.72	1.95	1.24
	D	1.81	1.86	1.92	1.96	1.32
Torino N45-024	A	1.84	1.89	1.93	1.96	1.30
	B	1.85	1.89	1.93	1.95	1.18
	C	1.78	1.88	1.90	1.94	1.26
	D	1.66	1.85	1.81	1.79	1.21
Vienna N48-181	A	1.83	1.87	1.89	1.95	1.23
	B	1.88	1.85	1.93	1.96	1.25
	C	1.85	1.82	1.89	1.94	1.29
	D	1.73	1.80	1.93	1.90	1.16
Zurich N47-377	A	1.63	1.79	1.75	1.91	1.24
	B	1.79	1.88	1.90	1.95	1.17
	C	1.68	1.81	1.84	1.91	1.20
	D	1.78	1.87	1.83	1.96	1.19

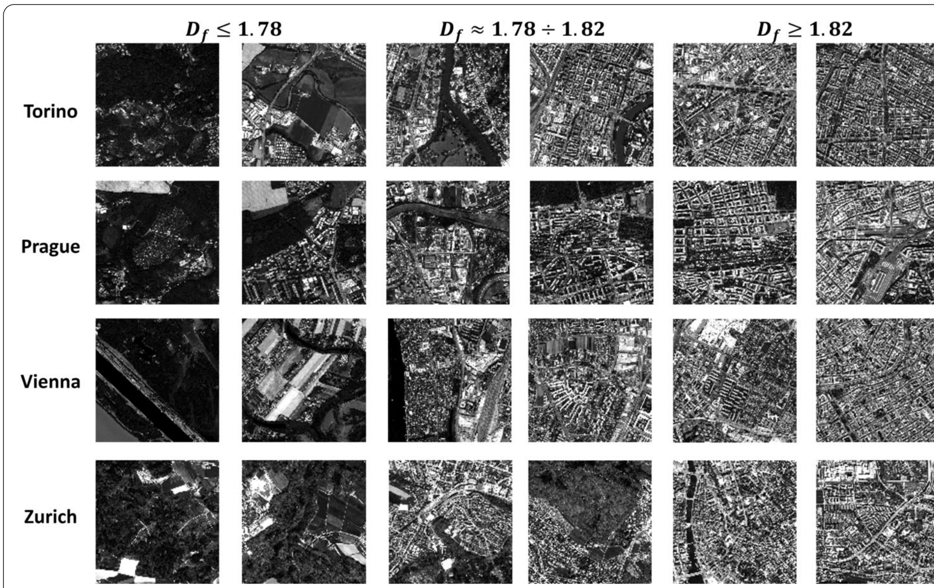

Figure 7 Comparison of different urban areas from four cities (Torino, Prague, Vienna, and Zurich) characterized by similar D_f values. Despite variations in morphology and urban structure, the relationship between the degree of urbanization and the corresponding D_f value appears consistent and well correlated. This suggests that the H values predicted by **RegFractNet** related with the fractal dimension D_f captures underlying structural properties of urban patterns regardless of the specific city context

sharing similar D_f values, also exhibit comparable structural characteristics, despite differences in geographical location and specific urban layouts. In particular, higher fractal dimensions ($D_f \geq 1.82$) are associated with densely built environments, characterized by irregular patterns and high morphological complexity typical of consolidated urban cores.

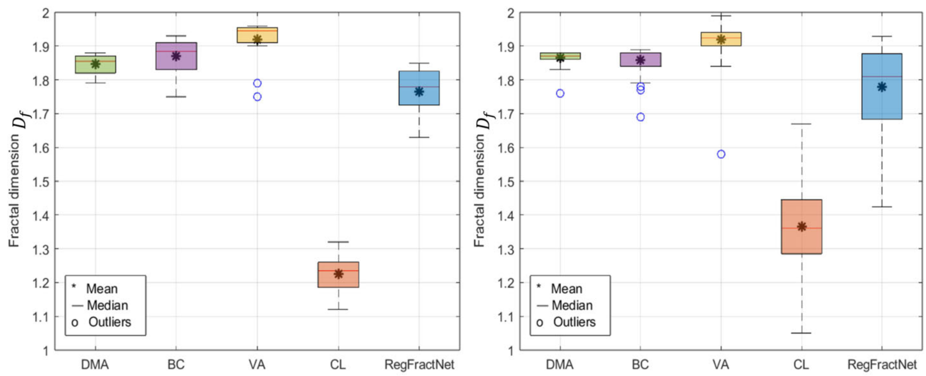

Figure 8 Fractal dimensions (mean, median and outliers) obtained by **RegFractNet** and Standard methods. (Left Panel) 16 sub-areas of size 512 × 512 of the four cities (Torino, Prague, Vienna, and Zurich); (Right Panel) 64 sub-areas of size 128 × 128 of one city (Torino)

Intermediate values ($D_f \approx 1.78 \div 1.82$) correspond to transitional zones, where mixed land use, partial fragmentation, and moderate spatial organization are observed. Lower fractal dimensions ($D_f \leq 1.78$) are mostly linked to less urbanized or peri-urban areas, where spatial patterns become more homogeneous and less complex, often reflecting vegetation or sparse development.

The box-plot results in Fig. 8 related to Tables 1 and 2, indicate that **RegFractNet** provides Hurst exponent estimates that are consistent with standard approaches, supporting its validity as a data-driven alternative. Traditional methods, particularly VA, tend to yield higher mean values and low dispersion, suggesting possible overestimation and limited sensitivity to spatial variability. **RegFractNet** and CL (with a different range of fractal dimension estimations) exhibit greater dispersion, reflecting an enhanced ability to capture heterogeneity in urban areas. Regarding the inherent variability across standard methods, it is worth clarifying that even with correct estimates of the Hurst exponent, they are inherently different due to underlying distinct metrics and parameters. **RegFractNet** not only predicts the Hurst exponent values but also exhibits a more consistent and broader dynamic range across different urban morphologies, as well as higher sensitivity (particularly on small patches of 128×128 pixels) where few data are available.

An *Agreement Plot* based on the Bland-Altman analysis [29] is shown in Fig. 9 to compare estimates related to the same variable. The Bland–Altman approach reveals a low difference between the **RegFractNet** and DMA methods (left panel Fig. 9). The negative bias (–0.0806) indicates that **RegFractNet** underestimates the fractal dimension compared to DMA. The limits of agreement (–0.1990 to 0.0377) span 0.2367. The Bland-Altman analysis (right panel Fig. 9) shows the mean bias to be –0.0883, the standard deviation of differences is 0.1031, and the 95% limits of agreement range from –0.2903 to 0.1137, giving a total amplitude of approximately 0.404. Hence, it is moderate but larger than in the previous 16-sample analysis, reflecting greater heterogeneity across a broader set of image patches.

5 Conclusion and future work

Fractal geometry offers a powerful perspective and unifying mathematical framework for understanding urban scaling laws. By relating Hurst exponent and fractal dimensions of

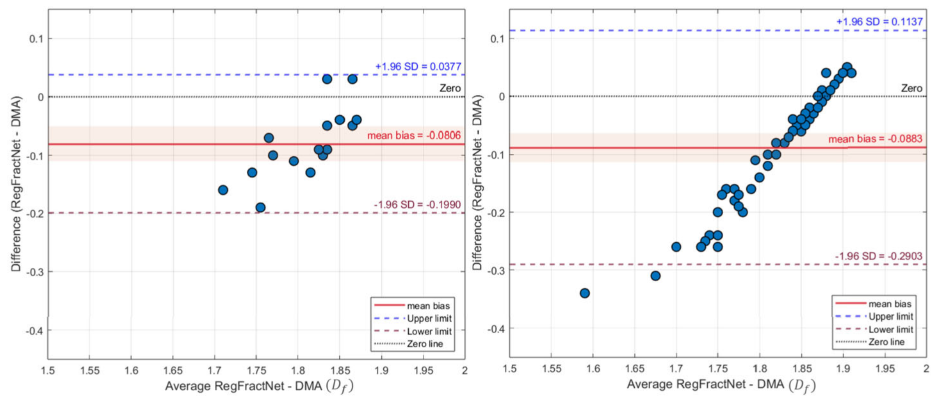

Figure 9 Bland-Altman analysis comparing the fractal dimension derived from the Hurst exponent estimated by the **RegFractNet** and DMA methods. The plots show the difference between the two methods against their average, with the bias, 95% limits of agreement, and the zero line. For detailed numerical results, see Table 1 and 2. (Left panel) Values derived from a total of 16 sectors distributed across four European cities: Torino, Prague, Vienna, and Zurich from WV-2 imagery. (Right panel) Values derived from a total of 64 fixed-size non-overlapping patches, extracted from Torino city

population distributions, one can describe the scaling of infrastructure and social interaction networks [7, 8]. The way cities grow and occupy space via the addition of fractal pattern units could consistently explain the scaling behaviors of several socio-technical urban features. In this context, computational methods are increasingly adopted to quantify urban patterns in terms of Hurst exponents, which depend upon blocks, building and road distributions detected by satellite sensors.

In this work we have put forward **RegFractNet**, a CNN-based regression model, able to predict the Hurst exponent of urbanized areas from WorldView-2 (WV-2) satellite images. The network model is trained on synthetic images of Brownian surfaces to yield a continuous numerical output corresponding to the Hurst exponent value of the input image. The proposed network is able to classify urban regions based on their morphological complexity and also to assign Hurst exponent values that accurately correlate with the urbanization level. This behavior reflects how the network captures self-similarity and roughness patterns characteristic of urban surfaces, providing the corresponding urban fractal dimension for each surface. The **RegFractNet** deep learning model has been tested on diverse satellite image datasets, demonstrating its effectiveness as an urban descriptor for quantifying levels of urbanization [30]. Noticeably, unlike standard algorithms, **RegFractNet** estimates the Hurst exponent H from smaller size images (128 × 128 pixels) without requiring to partition the data matrix in subunits/boxes at varying scales.

Accurate estimates of fractal features are essential within the broader theoretical and computational framework of urban scaling laws for predicting social, spatial, and infrastructural properties and enabling the development of planning strategies specifically tailored to each city. Future work aims to train neural networks on larger Brownian surface datasets (512 × 512 and 1024 × 1024 pixels), to process higher-resolution images and increase the accuracy of the Hurst exponent of larger urban and periurban areas with increasing spatial complexity. The approach has the potential to improve the quantitative analysis of urban morphology and contribute to the fractal characterization of urban environments by exploiting the richness of satellite imagery datasets.

Abbreviations
CNN, Convolutional Neural Network; FBM, Fractional Brownian Motion; DMA, Detrending Moving Average; BC, Box Counting; VA, Variogram; CL, Climacogram; MSE, Mean Squared Error; CLF, Cholesky-Levinson Factorization; WV-2, WorldView-2; RoI, Region of Interest.

Supplementary information

Supplementary information accompanies this paper at https://doi.org/10.1140/epjds/s13688-026-00660-3.

Additional file 1. (PDF 17.1 MB)

Acknowledgements
A. Delgadillo-Jiménez (CVU No. 1323784) and A. Aguilar-Vallejo (CVU No. 541295) express gratitude to the Secretaría de Ciencias, Humanidades, Tecnología e Innovación (SECIHTI) for the PhD's scholarship. We also acknowledge support from the Government of the State of Hidalgo through the Consejo de Ciencia, Tecnología e Innovación de Hidalgo (CITNOVA) through the agreement CITNOVA/DByP/CAR/110/2024 for the scholarship "Becas de apoyo para estancias cortas de Maestría y Doctorado en Instituciones Nacionales y en el Extranjero". The authors thanks the European Space Agency (ESA) for granting access to the WorldView satellite imagery for the Politecnico di Torino.

Author contributions
Investigation, Conceptualization and Methodology, C.T.Q, A.D.J., R.C.O., A.A.V., A.P.V. and A.C.; C.T.Q, A.D.J., A.C. and R.C.O. wrote the main manuscript text; A.D.J., A.C. and R.C.O. prepared figures; All authors have read and agreed to the published version of the manuscript.

Funding information
The authors declare to have no financial support.

Data Availability
The data that support the findings of this study are available from WorldView-2 [17] but restrictions apply to the availability of these data, which were used under license for the current study, and so are not publicly available. Data are however available from the authors upon reasonable request and with permission of European Space Agency (ESA).

Declarations

RegFractNet model availability
The *RegFractNet* model has been made publicly available and can be accessed both via an interactive web application and a MATLAB plug-in at https://sites.google.com/view/lvc-upt/available-plugins. For any questions, technical doubts, or further assistance regarding the implementation and use of these tools, readers are encouraged to contact the corresponding author.

Ethics approval and consent to participate
Not applicable.

Consent for publication
Not applicable.

Competing interests
The authors declare no competing interests.

Author details
[1]Computer Vision Laboratory, Universidad Politécnica de Tulancingo, Ingenierías 100, Hidalgo, 43629, Mexico.
[2]Department of Applied Science and Technology (DISAT), Politecnico di Torino, Corso Duca degli Abruzzi, 24, Torino, 10129, Italy.

Received: 30 July 2025 Accepted: 28 April 2026 Published online: 13 May 2026

References
1. Batty M, Longley PA (1987) Fractal-based description of urban form. Environ Plan B, Plan Des 14(2):123–134
2. Batty M (1991) In: Crilly AJ, Earnshow RA, Jones H (eds) Cities as fractals: simulating growth and form. Springer, New York, pp 43–69
3. Frankhauser P (1998) The fractal approach: a new tool for the spatial analysis of urban agglomerations. Population 10(1):205–240
4. Bettencourt L, et al (2007) Growth, innovation, scaling, and the pace of life in cities. Proc Natl Acad Sci 104(17):7301–7306
5. Arvidsson M, Lovsjö N, Keuschnigg M (2023) Urban scaling laws arise from within-city inequalities. Nat Hum Behav 7(3):365–374
6. Bettencourt LM (2013) The origins of scaling in cities. Science 340(6139):1438–1441
7. Ribeiro FL, Meirelles J, Ferreira FF, Neto CR (2017) A model of urban scaling laws based on distance dependent interactions. R Soc Open Sci 4(3), 160926

8. Molinero C, Thurner S (2021) How the geometry of cities determines urban scaling laws. J R Soc Interface 18(176), 20200705
9. Carbone A, Murialdo P, Pieroni A, Toxqui-Quitl C (2022) Atlas of urban scaling laws. J Phys Complex 3(2), 025007
10. Gneiting T, Schlather M (2004) Stochastic models that separate fractal dimension and the Hurst effect. SIAM Rev 46(2):269–282
11. Goodchild MF, Mark DM (1987) The fractal nature of geographic phenomena. Ann Assoc Am Geogr 77(2):265–278. https://doi.org/10.1111/j.1467-8306.1987.tb00158.x
12. Martino GD, Iodice A, Riccio D, Ruello G, Zinno I (2018) The role of resolution in the estimation of fractal dimension maps from SAR data. Remote Sens 10. https://doi.org/10.3390/rs10010009
13. Granik N, et al (2019) Single-particle diffusion characterization by deep learning. Biophys J 117(2):185–192
14. Wentao H, Shaojuan M (2024) Deep learning for parameter identification of nonlinear dynamical system driven by fractional Brownian motion. Res Sq. https://doi.org/10.21203/rs.3.rs-5663187/v1
15. Valle D, Wagemakers A, Daza A, Sanjuán MA (2022) Characterization of fractal basins using deep convolutional neural networks. Int J Bifurc Chaos 32(13), 2250200
16. RegFractNet (2026) The CNN package and data used in this work are available at https://sites.google.com/view/lvc-upt/available-plugins. Last visit on 03/2026
17. WorldView-2 (2025) The ESA third party mission collection of the largest European urban areas recorded by the WorldView-2 satellite. Available at https://tpm-ds.eo.esa.int/oads/access/collection/WorldView-2. Last visit on 03/2025
18. Alzubaidi L, Zhang J, Humaidi AJ (2021) Review of deep learning: concepts, CNN architectures, challenges, applications, future directions. J Big Data 8:53
19. The MathWorks Inc. (2023) MATLAB version: 23.2.0.2485118 (R2023b) Update 6. The MathWorks Inc. Available at https://www.mathworks.com. Last visit on 10/2025
20. Sun Z (2022) Pattern recognition in convolutional neural network (CNN). In: ICMMIA 2022: application of intelligent systems in multi-modal information analytics, pp 295–302
21. FRACLAB (2025) We use the CLF algorithm included in the package FRACLAB. Available at https://project.inria.fr/fraclab/. Last visit on 05/2025
22. Carbone A (2007) Algorithm to estimate the Hurst exponent of high-dimensional fractals. Phys Rev E (3) 76(5), 056703
23. Moisy F (2025) boxcount. MATLAB Central File Exchange. Available at https://www.mathworks.com/matlabcentral/fileexchange/13063-boxcount. Last visit on 12/2025
24. Develi K, Babadagli T (1998) Quantification of natural fracture surfaces using fractal geometry. Math Geol 30:971–998
25. Dimitriadis P, et al (2019) Stochastic investigation of long-term persistence in two-dimensional images of rocks. Spat Stat 29:177–191
26. Thomas I, Frankhauser P, Keersmaecker ML (2007) Fractal dimension versus density of the built-up surfaces in the periphery of Brussels. Pap Reg Sci 86(2):287–307. https://doi.org/10.1111/j.1435-5957.2007.00122.x
27. Lagarias A, Prastacos P (2017) Estimation of fractal dimensions of Mediterranean cities using data for different built-up densities. In: ERSA-GR conference: cities and regions in a changing Europe: challenges and prospects, pp 5–7
28. Delgadillo A, Toxqui C, Aguilar A, Castro R, Padilla A, Carbone A (2025) Estimation of urban fractal dimension using a convolutional neural network. In: Lectures notes on artificial intelligence, vol 16221. Springer, pp 1–12
29. Karun MK, Puranik A (2021) BA.plot: an R function for Bland-Altman analysis. Clin Epidemiol Glob Health 12, 100831. https://doi.org/10.1016/j.cegh.2021.100831
30. Toxqui C, Padilla A, Delgadillo A, Aguilar A, Castro R, Carbone A (2025) Deep learning in urban studies through multi-spectral satellite imagery (invited paper). Future sensing technologies, vol 13710. SPIE, Bellingham, p 137100

Publisher's note